# **Energy &** Environmental Science



PAPER

**View Article Online** 



Cite this: Energy Environ. Sci., 2021. 14. 2394

Received 9th November 2020, Accepted 25th February 2021

DOI: 10.1039/d0ee03553j

rsc li/ees

## Novel Cu(Zn)-Ge-P compounds as advanced anode materials for Li-ion batteries†

Wenwu Li,\*ab Pengfei Shen,b Lufeng Yang,c Anjie Chen,d Jeng-Han Wang, od Yunyong Li, Db Hailong Chen Cand Meilin Liu +a

Both electronic and ionic conductivities are of high importance to the performance of anode materials for Li-ion batteries. Many large capacity anode materials (such as Ge) do not have sufficiently high electronic and ionic conductivities required for high-rate cycling. Here, we report a novel ternary compound, copper germanium phosphide (CuGe<sub>2</sub>P<sub>3</sub>), as a high-rate anode. Being synthesized via a facile and scalable mechanochemistry method, CuGe<sub>2</sub>P<sub>3</sub> has a cation-disordered sphalerite structure and offers higher ionic and electronic conductivities and better tolerance to volume change during cycling than Ge, as confirmed by first principles calculations and experimental characterization, including high-resolution synchrotron X-ray diffraction, HRTEM, SAED, XPS and Raman spectroscopy. Furthermore, the results suggest that CuGe<sub>2</sub>P<sub>3</sub> has a reversible Li-storage mechanism of conversion reaction. When composited with graphite by virtue of a two-stage ball-milling process, the yolk-shell structure of the amorphous carbon-coated CuGe<sub>2</sub>P<sub>3</sub> nanocomposite (CuGe<sub>2</sub>P<sub>3</sub>/C@Graphene) delivers a high initial coulombic efficiency (91%), a superior cycling stability (1312 mA h  $\rm g^{-1}$  capacity after 600 cycles at 0.2 A  $\rm g^{-1}$  and 876 mA h  $\rm g^{-1}$ capacity after 1600 cycles at 2 A  $g^{-1}$ ), and an excellent rate capability (386 mA h  $g^{-1}$  capacity at 30 A  $g^{-1}$ ), surpassing most Ge-based anodes reported to date. Moreover, a series of cation-disordered new phases in the Cu(Zn)-Ge-P family with various cation ratios offer similar Li-storage properties, achieving high reversible capacities with high initial coulombic efficiencies and desirable redox chemistry with improved safety.

#### **Broader context**

Electrode materials of high-power and energy density are required for the development of high-performance batteries to power portable electronics and electrical vehicles. While Ge anodes have a volumetric capacity similar to that of Si and higher ionic and electronic conductivity than Si, their practical application to lithium batteries is hindered by the large volume change during cycling and the high cost of Ge. Multi-phase composite anodes have attracted much attention due to the reversible synergistic effects of the constituent phases of the composites during cycling, which enhance the energy density, cycling life, and rate performance, compared to the unary or binary phase materials. However, the construction of desirable nanocomposite electrodes still faces many challenges such as thermodynamic metastability and complex surface/interface compatibility of the constituent phases. Thus, rational design and cost-effective fabrication of multi-phase nanocomposites with superior electrochemical Li-storage performance is of vital importance and great value to the research and development of a new-generation Li-ion batteries.

#### Introduction

Lithium-ion batteries (LIBs) have attracted extraordinary attention for many emerging applications, from portable devices to electric vehicles. However, the existing LIBs are still unable to meet the ever-increasing demand, and further improvement is needed to achieve higher gravimetric and volumetric energy densities and a longer service life. Electrode materials based on alloy-type reactions are often able to accommodate several Li ions and electrons per host atom, offering a high capacity. In particular, Si, Ge, and binary Si<sub>x</sub>Ge<sub>1-x</sub> alloys are regarded as potential alternatives to the

<sup>&</sup>lt;sup>a</sup> School of Materials Science & Engineering, Georgia Institute of Technology, Atlanta, GA, 30332, USA. E-mail: meilin.liu@mse.gatech.edu

<sup>&</sup>lt;sup>b</sup> School of Materials and Energy, Guangdong University of Technology, Guangzhou, 510006, P. R. China. E-mail: wenwuli@gdut.edu.cn

<sup>&</sup>lt;sup>c</sup> The Woodruff School of Mechanical Engineering, Georgia Institute of Technology, 771 Ferst Drive, Atlanta, GA, 30332, USA

<sup>&</sup>lt;sup>d</sup> Department of Chemistry, National Taiwan Normal University, Taipei, 11677, Taiwan

<sup>†</sup> Electronic supplementary information (ESI) available. See DOI: 10.1039/ d0ee03553i

widely used graphite anodes, chiefly due to their rather large Li-storage capacity (3578 mA h g<sup>-1</sup> capacity for Li<sub>15</sub>Si<sub>4</sub> and 1385 mA h g<sup>-1</sup> capacity for Li<sub>3.75</sub>Ge). The high volumetric capacities (9781 and 8645 mA h cm<sup>-3</sup> for Si and Ge anodes, respectively, compared with 790 mA h cm<sup>-3</sup> for graphite) also represent a significant advantage. Although Ge has greater electronic and Li-ionic conductivities than its Si counterparts, 1-4 the inherent electronic and Li-ionic conductivities still need to be significantly enhanced to achieve ultrahigh rate performance. In addition, the large volume variation during cycling usually results in the growth of variable solid electrolyte interphase (SEI) films as well as in a severe electronic contact loss of electrodes, thus leading to a relatively low initial coulombic efficiency and fast capacity decay.5

To overcome the aforementioned challenges while simultaneously enhancing Li-storage performance of alloy anode materials, various advanced nanostructures have been studied. 6-14 Nanosizing was demonstrated to be an effective strategy to the issues associated with extensive volume change. The open space within these nanostructures effectively accommodates the volume changes of the alloy-type anode materials during cycling, thus delaying the eventual capacity decay. However, most of these strategies require rather complex synthesis methods. In addition, nanosizing inevitably decreases the tapping density and hence the volumetric capacity of the electrode. Therefore, it is critical to keep a high packing density of the active material particles while ensuring an efficient electronic and ionic conduction throughout the electrode.

To significantly enhance inherent electronic and Li-ionic conductivities of Ge, researchers resorted to atomic substitution or doping  $^{15-24}$  in searching for new binary  $^{25-29}$  and ternary Ge-based anode materials.<sup>30-34</sup> For example, Se-doped Ge microparticles with a high tap density achieved high rate performance and long cycling stability of over 1000 cycles, profiting from not only the significantly improved electronic and Li-ionic conductivities but also the highly Li-permeable amorphous Li-Ge-Se inactive phase formed during cycling, which is responsible for alleviating strain and enhancing Li-ionic diffusion rate. 16 The ternary metal germanium oxides/chalcogenides are attractive for electrochemical energy storage applications since there exists a possible synergistic effect of the electroactive multi-components endowed by their outstanding physical, chemical, thermal and electronic properties. 35-38 More interestingly, Si-doped ternary Zn<sub>2</sub>GeO<sub>4</sub> compound effectively suppresses volume change, thus demonstrating a large capacity of 1274 mA h g<sup>-1</sup> at 200 mA g<sup>-1</sup> after 700 cycles as well as robust cycle stability of 2000 cycles at 5 A  $g^{-1}$  with a capacity decay ratio of 0.008% per cycle. The excellent performance mainly benefits from the substitution of the Si atom. This substitution imparts to the Zn<sub>2</sub>GeO<sub>4</sub> compound both high reactivity and reversibility as well as stress-relieved merits during discharge, as validated using first-principles calculations.<sup>37</sup> Unfortunately, the above ternary materials present compromised Li-storage performance because electrochemically derived products usually differ from each other in working potentials, thus showing a multi-stage redox chemistry. Moreover, most capacity contributions of ternary metal germanium oxides and sulfides are corresponded to the working potentials above 1.0 V, thus leading to a relatively low

energy density. Compared with oxides/chalcogenides, phosphides have higher energy efficiency and larger theoretical reversible capacity benefiting from the lower formation energy of Li<sub>3</sub>P compared with that of Li<sub>2</sub>O.<sup>39,40</sup> Nevertheless, to our best knowledge, there are no ternary metal germanium phosphides reported for electrochemical energy-storage as it is quite challenging to synthesize these ternary metal germanium phosphides by a facile method resulting from their thermodynamic meta-stability. Thus, designing metal germanium phosphides rationally with right chemistry as well as appropriate working potentials needs fundamental insights into the structure-performance relationship, which is urgent and extremely important to the research and development for a new battery technology.

Here, we report the successful co-integration of Cu and P into Ge to synthesize a novel ternary copper germanium phosphide, CuGe<sub>2</sub>P<sub>3</sub>. High-resolution synchrotron X-ray diffraction (XRD) and refinement, and first-principles calculations demonstrate that the as-synthesized CuGe<sub>2</sub>P<sub>3</sub> features cation-disorder and has faster electronic and Li-ionic conductivities and greater tolerance against volume variation, compared with their Ge counterparts. As an anode of LIBs, the as-synthesized CuGe<sub>2</sub>P<sub>3</sub> offers a large reversible capacity of 1457 mA h g<sup>-1</sup> with an initial coulombic efficiency up to 92% and a reasonable working potential of 0.5 V based on a reversible Li-storage mechanism of conversion reactions, as confirmed by various characterizations and electrochemical measurements. After the two-stage ball milling of CuGe<sub>2</sub>P<sub>3</sub> with graphite, CuGe<sub>2</sub>P<sub>3</sub>/C@Graphene shows a long cycling stability (1312 mA h g<sup>-1</sup> capacity after 600 cycles at 200 mA g<sup>-1</sup>, and 876 mA h g-1 capacity after 1600 cycles at 2 A g-1) and an ultrahigh rate performance (386 mA h g<sup>-1</sup> capacity at 30 A g<sup>-1</sup>). Furthermore, we extend CuGe<sub>2</sub>P<sub>3</sub> into a novel series of cationdisordered Cu(Zn)-Ge-P compounds with a large range of cationic ratios, which also present large capacities with high initial coulombic efficiency and suitable working potentials, thus further demonstrating their high promise as the next-generation high-performance anode materials for LIBs.

## Results and discussion

The complete Si-Ge solid solution with Ge-like atomic arrangement<sup>20–24</sup> wins a significantly superior Li-storage performance to the related single-component Ge anodes. Broadly, A<sup>II</sup>B<sup>IV</sup>C<sub>2</sub><sup>V</sup> and AIB2VC3 compounds with a wide range of valences also own a similar crystal structure. However, their Li-storage performance is rarely reported due to the complex synthetic conditions. Herein, we have obtained CuGe<sub>2</sub>P<sub>3</sub> by means of a simple and scalable mechanical ball milling method at room temperature under atmospheric pressure, thus saving the traditional chemical vapor transportation technique at high-temperature and high-pressure. 29-31 The synthetic process is schematically illustrated in Fig. 1a. To track the synthetic process, we collect the intermediate products at a predetermined ball milling time. As shown in Fig. 1b, after milling for 10 min, the fingerprint diffraction peaks for the raw materials of Cu, amorphous red P, and Ge still co-existed; at 0.5 h, the diffraction peaks of Cu and

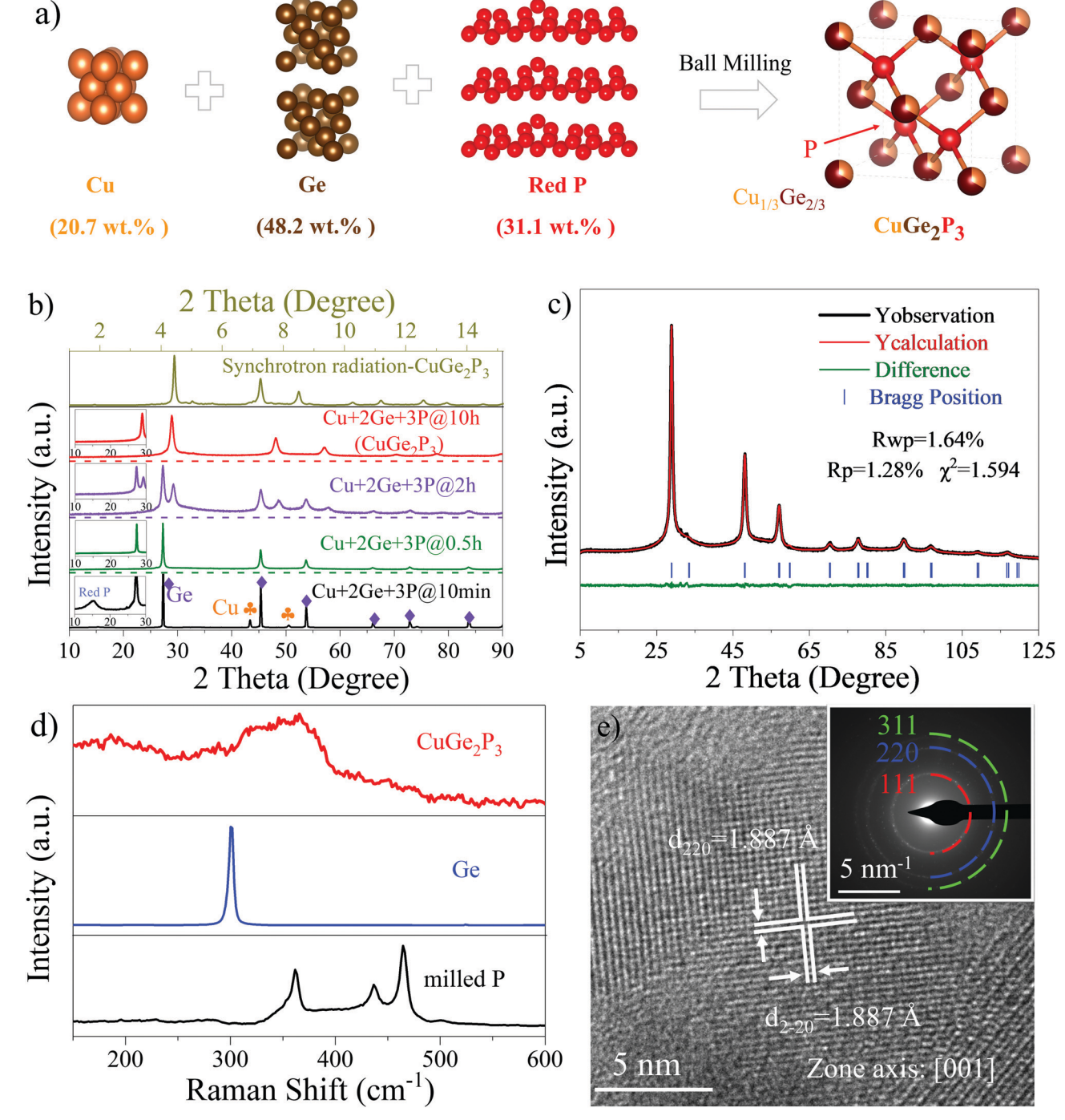


Fig. 1 (a) Schematically illustrated preparation procedure of the cation-disordered CuGe<sub>2</sub>P<sub>3</sub> compound; (b) evolved X-ray diffraction patterns (XRD) of Cu + 2Ge + 3P samples (Cu + 2Ge + 3P@x h means milling at x h, x = 1/6, 0.5, 2, 10); (c) XRD refinement of the above synthesized Cu + 2Ge + 3P@10hsample; (d) Raman spectroscopy of the above-synthesized cation-disordered CuGe<sub>2</sub>P<sub>3</sub> sample, milled P and Ge powders; and (e) high-resolution transmission electron microscopy (HRTEM) image along with the selected area electron diffraction (SAED; the inset at top right) pattern of the abovesynthesized cation-disordered CuGe<sub>2</sub>P<sub>3</sub>.

amorphous red P disappeared; at 2 h, a ternary phosphide of CuGe<sub>2</sub>P<sub>3</sub> appeared regardless of the residual Ge. After milling of 10 h or longer, we obtained the pure CuGe<sub>2</sub>P<sub>3</sub> with a Ge-like XRD pattern. To determine the structural parameters of the newly synthesized phase, we resorted to the XRD refinement (Fig. 1c) of the as-synthesized CuGe<sub>2</sub>P<sub>3</sub>. As depicted in Fig. 1a, the model

cell can be well-assigned to the cation-disordered sphalerite structure, where Cu and Ge replace the Zn site randomly at the given mole ratio of 1:2 and P occupies the S site completely. Detailed crystallographic data are given in Tables S1 and S2 (ESI†). Furthermore, the cation-disordered crystal structure of the sample was characterized by high-resolution synchrotron X-

ray diffraction (Fig. 1b, top and Table S3, ESI†); the results suggest that no impure phases were detected after milling for 10 h, with the only phase being the newly synthesized cation-disordered CuGe<sub>2</sub>P<sub>3</sub>. To observe the detailed morphology, we performed field-emission scanning emission microscopy (FESEM) and low-magnification transmission electron microscopy (TEM) measurements. As shown in Fig. S1 (ESI†), the CuGe<sub>2</sub>P<sub>3</sub> sample is composed of microsized secondary particles, which consist of numerous aggregated primary nanoparticles. To precisely control the particle size or morphology, the ternary Cu-Ge-P compounds may be synthesized by the phosphatization of the ternary Cu-Ge-O compounds with different morphologies. The Cu-Ge-P compounds may also be synthesized using a wet chemical method such as solvothermal reaction of copper salts, germanium salts or oxides and organic phosphorus sources. To probe more detailed information on the microstructure, we further characterized the as-synthesized CuGe<sub>2</sub>P<sub>3</sub> using high-resolution transmission electron microscopy (HRTEM, Fig. 1e), including selected area electron diffraction (SAED, the inset in the Fig. 1e). The measured zonal facets of  $(2\bar{2}0)$  and (220)along the [001] zone axis as well as the absence of diffraction rings associated with the cation-ordered superstructure further validate the cation-disordered sphalerite structure of the as-synthesized CuGe<sub>2</sub>P<sub>3</sub>. Additionally, the common Ge-like crystal plane of (111) is also observed as presented in Fig. S2 (ESI†). In addition, we also characterized Raman spectra of the cation-disordered CuGe<sub>2</sub>P<sub>3</sub>. As shown in Fig. 1d and Fig. S3 (ESI†), its fingerprint peaks are completely different from those of the ball milled Ge and P, thus suggesting the formation of ternary CuGe<sub>2</sub>P<sub>3</sub>.

Encouraged by the cation-disordered structure and Li-storage components of Ge and P, we believe that the as-prepared ternary metal germanium phosphide of CuGe<sub>2</sub>P<sub>3</sub> would offer unparalleled Li-storage properties, compared with the single-component and binary compound anodes. The electrochemical Li-storage performance of the Cu + 2Ge + 3P samples corresponding to the above-analyzed XRD data as well as the milled Ge and P samples was evaluated. As shown in Fig. 2a, b and d, pure CuGe<sub>2</sub>P<sub>3</sub> shows the best Li-storage properties in terms of suitable working potential, small polarization loss, large reversible specific capacity and high initial coulombic efficiency. Specifically, the as-synthesized CuGe<sub>2</sub>P<sub>3</sub> shows a reversible capacity of 1457 mA h g<sup>-1</sup> with an initial coulombic efficiency up to 92%, and a suitable working potential of 0.5 V. It should be noted that although the intermediate Cu + 2Ge + 3P samples deliver obvious multi-stage Li-storage properties, the as-synthesized CuGe<sub>2</sub>P<sub>3</sub> shows relative smooth discharge-charge profiles, which favor the discharge depth control when applied in full cells. This phenomenon can be probably attributed to the difference in the electrochemical Li-storage process caused by the primary micro-structural difference of these materials. Fig. 2c and Fig. S4a, b (ESI†) show the initial cyclic voltammetry curves of the as-synthesized CuGe<sub>2</sub>P<sub>3</sub>, which are well-consistent with the redox potentials delivered by the initial dischargecharge profiles. During the first reduction process, there exist two reduction bands centered at 0.547 V and 0.183 V (vs. Li<sup>+</sup>/Li), which can be explained as a small amount of side reaction such as the formation of solid electrolyte interphase and then the Liionic uptake reaction of CuGe<sub>2</sub>P<sub>3</sub>. During the oxidation process,

there exist three oxidation peaks locating at 0.491 V, 0.861 V and 1.156 V, corresponding to Li-ionic extraction of binary Li-Ge, Li-P alloys and Li<sub>x</sub>CuGe<sub>2</sub>P<sub>3</sub>, respectively. During the subsequent reduction process, there exist three reduction peaks centered at 0.7 V, 0.5 V and 0.16 V, corresponding to the Li-ionic uptake and formation of Li<sub>x</sub>CuGe<sub>2</sub>P<sub>3</sub> as well as binary Li-P and Li-Ge alloys. Compared with the initial cycle, the subsequent cycles obtain the slightly reduced polarization, which mainly results from defects produced during the first discharge-charge process, leading to faster Li-ionic and electronic conductivities. It should be noted that compared with some P-based anodes, CuGe<sub>2</sub>P<sub>3</sub> presents a relatively low working potential, which may be attributed to the specific structure with different Li-ion diffusion paths and reaction mechanisms. 25,26,41 As observed in Fig. 2d and Fig. S4c (ESI†), the as-synthesized CuGe<sub>2</sub>P<sub>3</sub> delivers a large reversible capacity of 1457 mA h  $g^{-1}$  at 100 mA  $g^{-1}$  and can be cycled over 100 cycles without obvious decay, which is superior to other impure Cu + 2Ge + 3P samples as well as the milled Ge and P electrodes. Moreover, CuGe<sub>2</sub>P<sub>3</sub> shows a significantly improved rate performance (Fig. 2e), compared with that of milled Ge anodes. Even when cycled without any conductive agent, CuGe<sub>2</sub>P<sub>3</sub> can still deliver a large reversible capacity of 1260 mA h g<sup>-1</sup> with an initial coulombic efficiency up to 90% at 100 mA  $g^{-1}$  (Fig. S5, ESI†). The significantly enhanced rate capability of the as-prepared CuGe<sub>2</sub>P<sub>3</sub> anodes can be probably assigned to its much quicker Li-ionic and electronic transport kinetics compared with that of the Cu + 2Ge + 3P and Ge samples, which will be analyzed below.

Considering the as-synthesized CuGe<sub>2</sub>P<sub>3</sub> as a promising anode material for LIBs with superior electrochemical Li-storage performance in respect of large reversible capacity, high initial coulombic efficiency, high-rate performance and high energy efficiency, we further performed the ex situ high-resolution synchrotron X-ray diffraction, XRD, HRTEM along with SAED and FFT, Raman and XPS to characterize its structural evolution during the dischargecharge process. As shown in Fig. S6 (ESI†), the crystal structure of CuGe<sub>2</sub>P<sub>3</sub> owns enough space to accommodate up to three Li-ions within the tetrahedral sties surrounded by the occupied cationic and anionic sites in the sphalerite structure. As shown in Fig. S7 and S8 (ESI†), the energies associated with the insertion of Li ions into  $CuGe_2P_3$  to form  $Li_xCuGe_2P_3$  (x = 1/16 to 3) are all negative, confirming the probability of forming the Li<sub>x</sub>CuGe<sub>2</sub>P<sub>3</sub> (x < 3) phases during lithiation. As presented in Fig. 3a and  $b_1$ , b2, with a decrease in potential, the CuGe2P3 began to uptake Li-ions indicated by its gradual amorphization, where the XRD pattern features as no diffraction peaks. As lithiation continued, the amorphous electrode became crystalline Li<sub>2</sub>CuP and other amorphous products. We noted that the crystalline Li2CuP compound owns both Li-ionic and electronic conductivities, 42 simultaneously, which help to achieve an ultrahigh rate performance. When completely discharged to 5 mV, the electrode degraded into the almost amorphous mixture of Li<sub>3</sub>P, Li<sub>3.75</sub>Ge and Cu as co-confirmed by XRD (Fig. 3b<sub>5</sub>), the ex situ Raman (Fig.  $3c_4-c_6$ ), XPS (Fig.  $3d_3-f_3$ , and Fig. S10, ESI†), ex situ highresolution synchrotron X-ray diffraction (Fig. S11b, ESI†) and HRTEM image (Fig. S12-iii, ESI†) along with the corresponding FFT images. Our XPS analysis reveals that, compared with the

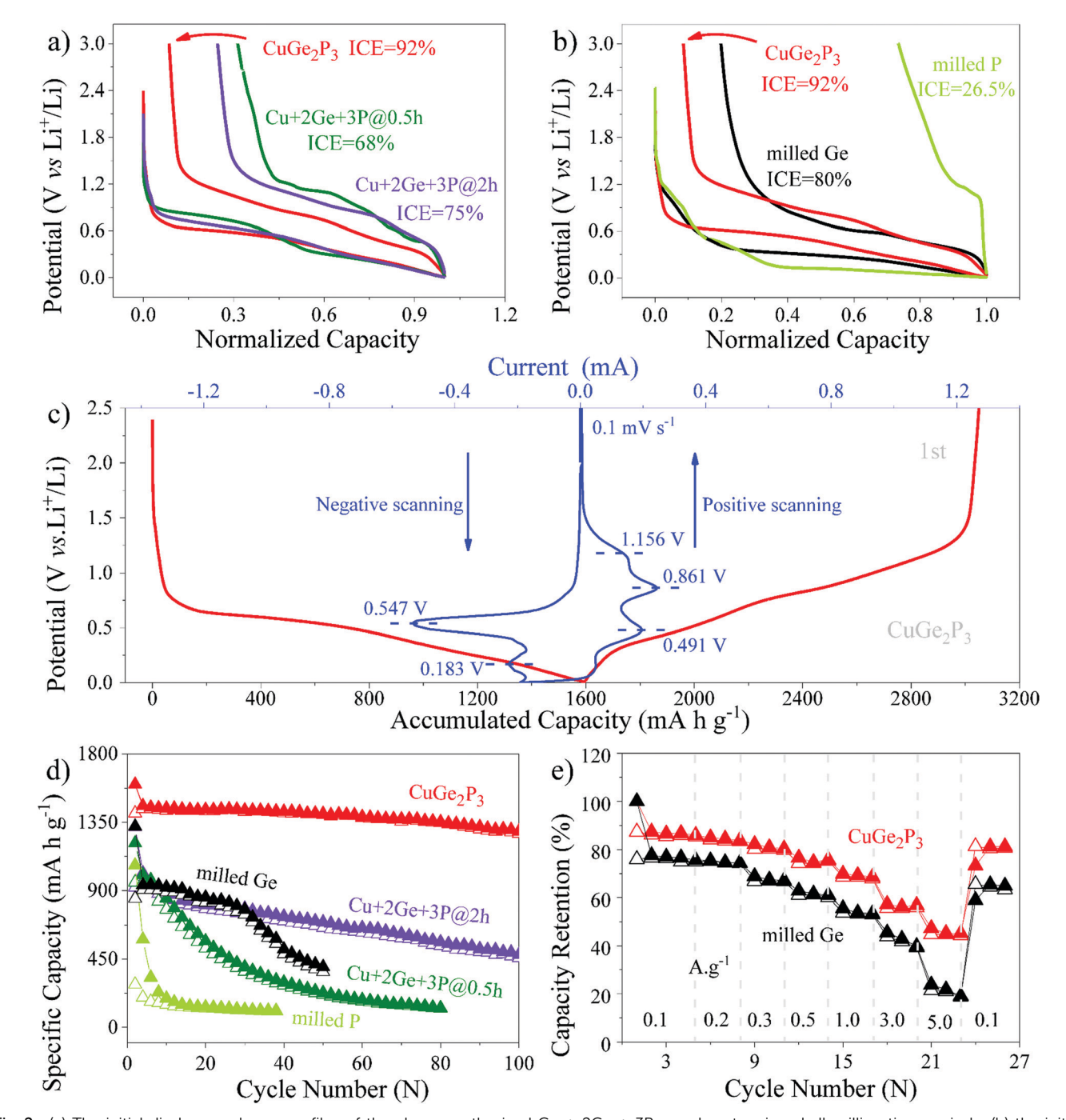


Fig. 2 (a) The initial discharge-charge profiles of the above-synthesized Cu + 2Ge + 3P samples at various ball-milling time periods; (b) the initial discharge-charge profiles of the above-synthesized cation-disordered CuGe<sub>2</sub>P<sub>3</sub>, milled P and milled Ge electrodes; (c) comparation of the initial cyclic voltammetry curves and first galvanostatic discharge-charge profiles for the above synthesized cation-disordered CuGe<sub>2</sub>P<sub>3</sub> electrodes; (d) cycling stability of the above-synthesized Cu + 2Ge + 3P samples at various ball-milling time periods and milled Ge electrodes; and (e) rate performance of the as-obtained CuGe<sub>2</sub>P<sub>3</sub> powder and milled Ge powder.

spectra for the pristine CuGe<sub>2</sub>P<sub>3</sub> and the mixed powder of Cu, Ge, and P, the peaks of  $Li_{15}Ge_4$  (26.95 eV, Fig. 3d<sub>3</sub>),  $Li_3P$  (127 eV, Fig. 3e<sub>3</sub>), and elemental Cu (932.85 eV, Fig. 3f<sub>3</sub>) appeared, implying the formation of these lithiation products. 43,44 When charged, the binary Li-M alloy products gradually disappeared and the crystalline Li<sub>2</sub>CuP appeared again (Fig. 3b<sub>7</sub> and Fig. S9, ESI†). When completely charged to 3.0 V, the electrode upgraded into

almost amorphous CuGe<sub>2</sub>P<sub>3</sub> as co-validated by Raman (Fig. 3c<sub>1</sub>-c<sub>2</sub> and  $c_8-c_9$ ), XPS (Fig.  $3d_4-f_4$  and Fig. S10, ESI†), the ex situ XRD (Fig. 3b<sub>9</sub>) and ex situ high-resolution synchrotron X-ray diffraction (Fig. S11a-ii, ESI†) along with HRTEM and SAED presented in Fig. S12-v (ESI†). It is noted that, compared with the fingerprint XPS signals of pristine crystalline CuGe<sub>2</sub>P<sub>3</sub>, the XPS signals of amorphous CuGe<sub>2</sub>P<sub>3</sub> after cycling were shifted

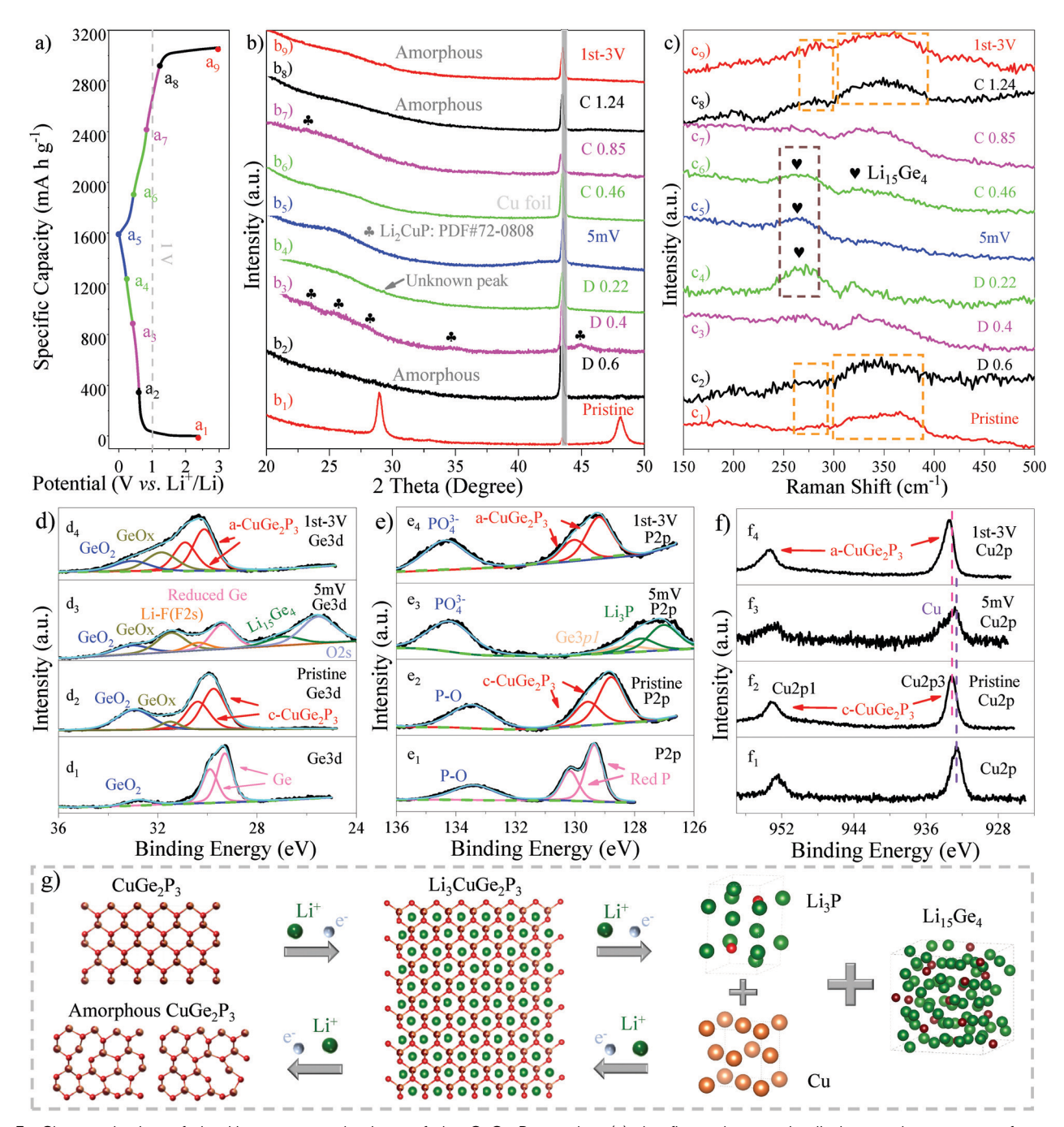


Fig. 3 Characterization of the Li-storage mechanisms of the  $CuGe_2P_3$  anodes: (a) the first galvanostatic discharge-charge curves for ex situ characterization at a current rate of 100 mA g<sup>-1</sup>; (b) ex situ XRD patterns corresponding to the indicators marked in (a); (c) ex situ Raman patterns corresponding to the indicators marked in (a); high resolution XPS spectra of the CuGe<sub>2</sub>P<sub>3</sub> electrode after cycling, pristine CuGe<sub>2</sub>P<sub>3</sub> powder and raw material of Ge, P or Cu: (d) Ge 3d; (e) P 2p; (f) Cu 2p; and (g) the scheme of the overall Li-storage process.

slightly to a higher binding energy, attributed to the amorphization.45 It should be also noted that the amorphization of the CuGe<sub>2</sub>P<sub>3</sub> anodes favors its cycling stability profiting from the uniform strain release during the repeated discharge-charge process.46 As schematically illustrated in Fig. 3g, Li-storage process of CuGe<sub>2</sub>P<sub>3</sub> is expressed using the following equations: During the Li-ionic uptake process:

$$CuGe_2P_3 + xLi^+ + xe^- \rightarrow Li_xCuGe_2P_3 (x < 3);$$
 (i)

$$\text{Li}_x\text{CuGe}_2\text{P}_3 + (16.5 - x) \text{Li}^+ + (16.5 - x) \text{e}^-$$
  
 $\rightarrow \text{Cu} + 2\text{Li}_{3.75}\text{Ge} + 3\text{Li}_3\text{P};$  (ii)

During the Li-ionic extraction process:

$$2\text{Li}_{3.75}\text{Ge} + \text{Cu} + 3\text{Li}_{3}\text{P} - (16.5 - x)\text{Li}^{+} - (16.5 - x)\text{ e}^{-}$$
  
 $\rightarrow \text{Li}_{x}\text{CuGe}_{2}\text{P}_{3};$  (iii)

$$\text{Li}_x\text{CuGe}_2\text{P}_3 - x\text{Li}^+ - x\text{e}^- \rightarrow \text{CuGe}_2\text{P}_3 \text{ (almost amorphous)};$$
(iv)

Total reaction:

$$CuGe_2P_3 + 16.5Li^+ + 16.5e^- \leftrightarrow Cu + 2Li_{3.75}Ge + 3Li_3P.$$
 (v)

According to the above reaction equations, the  $CuGe_2P_3$  electrode can store 16.5 Li-ions per formula unit, contributing to its theoretical capacity of 1467 mA h g $^{-1}$ , where Ge provides 667 mA h g $^{-1}$ , and P delivers 800 mA h g $^{-1}$ . As known, in electronic conductivity, Cu ranks only second to Au among various metals and thus is widely utilized as current collectors for anode materials of batteries. The endogenous nanoscale Cu during the deep discharge process contributes no capacity, but provides significantly enhanced electronic conductivity and acts as a physical barrier against electrochemical agglomeration. Moreover, fast charging always gives rise to an increase in the temperature of operating batteries; the formed Cu, as an excellent thermal conductor, will significantly alleviate the local overheating and act as a local thermal protection medium for LIBs.

To find the primary cause behind the superior Li-storage performance of the as-synthesized CuGe<sub>2</sub>P<sub>3</sub> to their Ge counterparts, we performed density functional theory calculations to unveil the Li-ionic and electronic transport kinetics, and resistance capability against volume change. Based on the cationdisordered structural characteristics, we made a recognized cation-disordered model presented in Fig. S13a (ESI†). Firstly, we calculated the electronic structure of CuGe<sub>2</sub>P<sub>3</sub> and Ge. Surprisingly, as presented in Fig. 4a, the total DOS value of the cation-disordered CuGe<sub>2</sub>P<sub>3</sub> crosses the Fermi level, giving the direct evidence for its electronic conductivity. This result is also well-consistent with the calculated band structure (Fig. S14, ESI†), which shows no band gap, also suggesting its metallic conductivity. As a comparison, Ge only has a semiconducting feature evidenced by its total DOS value equalling to zero at the Fermi level on the basis of the simulated electronic structure shown in Fig. 4a. This calculated result is also well-consistent with the literature published before. 47 The electronic conductivity of the as-prepared CuGe<sub>2</sub>P<sub>3</sub> can be probably attributed to the cation disorder. To validate DFT calculation results, namely, improved electronic transport kinetics of CuGe<sub>2</sub>P<sub>3</sub>, we carried out electrochemical impedance spectroscopy measurements to

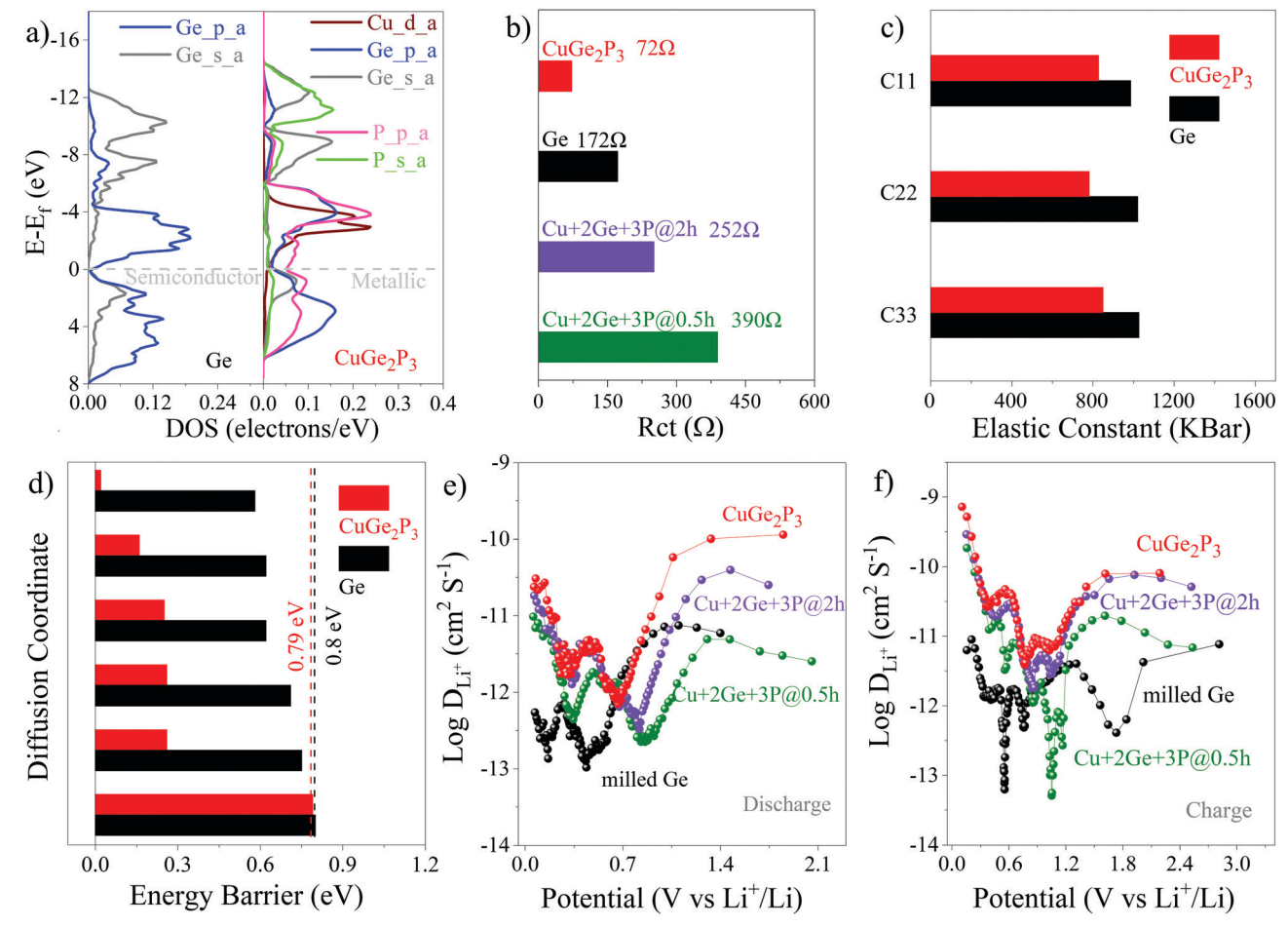


Fig. 4 (a) Density of state (DOS) of  $CuGe_2P_3$  and Ge; (b) charge transfer resistance ( $R_{ct}$ ) of Ge, as well as the above-synthesized Cu + 2Ge + 3P samples at various ball-milling time periods; (c) elastic constant of  $CuGe_2P_3$  electrode and Ge; (d) diffusion energy barrier of  $CuGe_2P_3$  and Ge; Diffusion coefficient of the above-synthesized Cu + 2Ge + 3P samples at various ball-milling time periods and milled Ge electrodes; (e) discharge and (f) charge.

obtain charge transfer resistance (R<sub>ct</sub>) of the CuGe<sub>2</sub>P<sub>3</sub> anodes. As presented in Fig. 4b and Fig. S15 (ESI†), the  $R_{\rm ct}$  value (72  $\Omega$ ) of the cation-disordered CuGe<sub>2</sub>P<sub>3</sub> is significantly smaller than those (172  $\Omega$ , 252  $\Omega$  and 390  $\Omega$  for Ge, Cu + 2Ge + 3P@2 h and Cu + 2Ge + 3P@0.5 h, respectively) of Ge and the ball milled intermediate Cu + 2Ge + 3P samples, thus validating that the assynthesized CuGe<sub>2</sub>P<sub>3</sub> owns the best electronic conductivity among these comparisons (Ge and the ball milled Cu + 2Ge + 3P samples). Moreover, we also measured the electrical conductivity of the CuGe<sub>2</sub>P<sub>3</sub>-based electrodes, the as-synthesized CuGe<sub>2</sub>P<sub>3</sub> powder, the mixed Cu + 2Ge + 3P powder, and the raw materials of Ge and P. As shown in Table S4 (ESI†), the electrical conductivities of the CuGe<sub>2</sub>P<sub>3</sub>-based electrode and the CuGe<sub>2</sub>P<sub>3</sub> powder are several orders of magnitude greater than those of the mixed Cu + 2Ge + 3P powder and the raw materials of Ge and P. Secondly, on Li-ionic storage and diffusion kinetics, we simulated various Li-ionic structural configurations by virtue of filling lithium atoms in the lattices or interstitial sites to optimize the structure featured by the lowest energy. The related lattices were relaxed via applying primary multiple energy minimization calculation principles. As illustrated in Fig. S6 (ESI†), there are three voids with enough space to host one Li atom per void, in the crystal structure of the as-synthesized CuGe<sub>2</sub>P<sub>3</sub>. We performed the Liionic transport activation energy calculation with a Li-ion hoping among the voids within the random-cation supercell (Fig. S13, ESI†). The Li-ionic diffusion paths follow octahedron-tetrahedron-octahedron sites (Fig. S16a, ESI†) in which every site is encompassed by Ge or Cu atoms. The related Li-ionic transport activation energy barriers are plotted in Fig. 4d. Most of the Li-ionic transport activation energy values of the cation-disordered CuGe<sub>2</sub>P<sub>3</sub> are below 0.26 eV. As a comparison (Fig. 4d and Fig. S16b, ESI†), however, most Li-ionic transport activation energies for Ge are over 0.62 eV. The smaller Li-ionic transport barriers of the cation-disordered CuGe<sub>2</sub>P<sub>3</sub> indicate its more facile Li-ionic transport kinetics, compared with that of its Ge counterparts. To validate the theoretical predictions, we carried out the galvanostatic intermittent titration measurement to evaluate and compare Li-ionic diffusion capability of the above-synthesized Cu + 2Ge + 3P samples and Ge electrodes. Li-ionic diffusion coefficients can be determined according to the following equation:

$$D = \frac{4}{\pi} \left( \frac{iV_{\rm m}}{Z_{\rm A}FS} \right)^2 \left( \frac{\mathrm{d}E/\mathrm{d}\sigma}{\mathrm{d}E/\mathrm{d}t^{1/2}} \right)^2$$

where D corresponds to Li-ionic diffusion coefficient, i represents current,  $Z_A$  is charge number ( $Z_A = 1$ ), F refers to Faraday constant of 96 485 C mol $^{-1}$ ,  $V_{\rm m}$  is the molar volume of electrodes, S stands for the geometric area of the electrode,  $dE/d\sigma$  is the slope of the coulomtric titration curve, found by plotting the steady state voltages E (V) measured after each titration step  $\sigma$ ; and dE/d $t^{1/2}$ is the slope of the linearized plot of the potential E(V) during the current pulse of duration t (s). As presented in Fig. 4e, f and Fig. S17 and S18 (ESI†), the average Li-ionic diffusion coefficients for the cation-disordered CuGe<sub>2</sub>P<sub>3</sub> at the operating potential are higher than those of the ball milled intermediate Cu + 2Ge + 3P samples and Ge electrode counterparts. Thirdly, we calculated the

mechanical properties of the cation-disordered CuGe<sub>2</sub>P<sub>3</sub> to evaluate its resistance capability against volume variation during repeated Li-ionic uptake-extraction process utilizing first-principles theory. As shown in Fig. 4c, the elastic constants of the as-prepared CuGe<sub>2</sub>P<sub>3</sub> are significantly smaller than those of their Ge counterparts, which suggests the cation-disordered CuGe<sub>2</sub>P<sub>3</sub> is much softer than Ge. The softer property means it favorably accommodates the volume variation caused by the repeated lithiationdelithiation of the host material as demonstrated in Fig. S19 (ESI†). To make a long story short, the cation-disordered CuGe<sub>2</sub>P<sub>3</sub> has significantly faster electronic and Li-ionic conductivities (Fig. 4a and d), as well as stronger resistance to structural change (Fig. 4c) compared with their Ge counterparts. These calculated results rationalize the Li-storage superiority of the cationdisordered CuGe<sub>2</sub>P<sub>3</sub> in terms of faster reaction kinetics, smaller polarization loss as well as higher energy efficiency compared with these ball milled intermediate Cu + 2Ge + 3P samples and Ge electrode counterparts.

To achieve the long-term cycling stability to the practical level, we construct the yolk-shell structured amorphous carbon coated CuGe<sub>2</sub>P<sub>3</sub> nanocomposite (CuGe<sub>2</sub>P<sub>3</sub>/C@Graphene) using a two-step mechanical ball milling of the lab-prepared CuGe<sub>2</sub>P<sub>3</sub> with low-cost layered graphite, as illustrated in Fig. 5a. In the first step, the particle size of CuGe<sub>2</sub>P<sub>3</sub> was significantly decreased into less than five nanometres and the particles were embedded into amorphous carbon (Fig. S20, ESI†) produced by the destroyed layered graphite during the high-energy ball milling process. In the second ball milling process, equal amount of layered graphite was poured into the above amorphous carbon coated CuGe<sub>2</sub>P<sub>3</sub>. After a further short milling time of 0.5 h, CuGe<sub>2</sub>P<sub>3</sub>/C@Graphene was formed. As shown in Fig. S21 (ESI†), the carbon content in the composite electrode is 22.69%, which is consistent with the predetermined weight ratio of graphite to CuGe<sub>2</sub>P<sub>3</sub> (2:7 or 22.2% graphite). The elemental mapping images (Fig. 5d-g and Fig. S22, ESI†) further demonstrate the morphology and distribution of CuGe<sub>2</sub>P<sub>3</sub> within the carbon shell. In the HRTEM image shown in Fig. 5c on the carbon shell, we observed the d-spacing of about 0.33 nm, corresponding to the abovementioned graphite sheets. The amorphous carbon matrix serves to activate and stabilize the interior of the composite, while the graphite sheets protect and restrain the exterior surface. 48 Benefiting from the synergistic combination of these two carbon components, CuGe<sub>2</sub>P<sub>3</sub>/C@Graphene achieved extremely stable cycling stability as well as outstanding rate performance. This morphology is also favorable when applied in batteries as the primary nanoparticles can promote the contact between the active materials and electrolytes, and reduce the Li-ionic diffusion path, while the secondary microsized particles can enhance the electrode density, which favors to obtain high volumetric energy density. When CuGe<sub>2</sub>P<sub>3</sub>/C@Graphene is used as anode materials for LIBs, the first three discharge-charge profiles (Fig. 6a) are well-matched with those of the pure cation-disordered CuGe<sub>2</sub>P<sub>3</sub> compound counterparts (Fig. 2d). Moreover, the CuGe<sub>2</sub>P<sub>3</sub>/C@Graphene presents 1312 mA h g<sup>-1</sup> capacity after 600 cycles with coulombic efficiency approaching to 100% at 0.2 A g<sup>-1</sup> as shown in Fig. 6c and Fig. S23 (ESI†), and the retained capacity is 91.3% of the

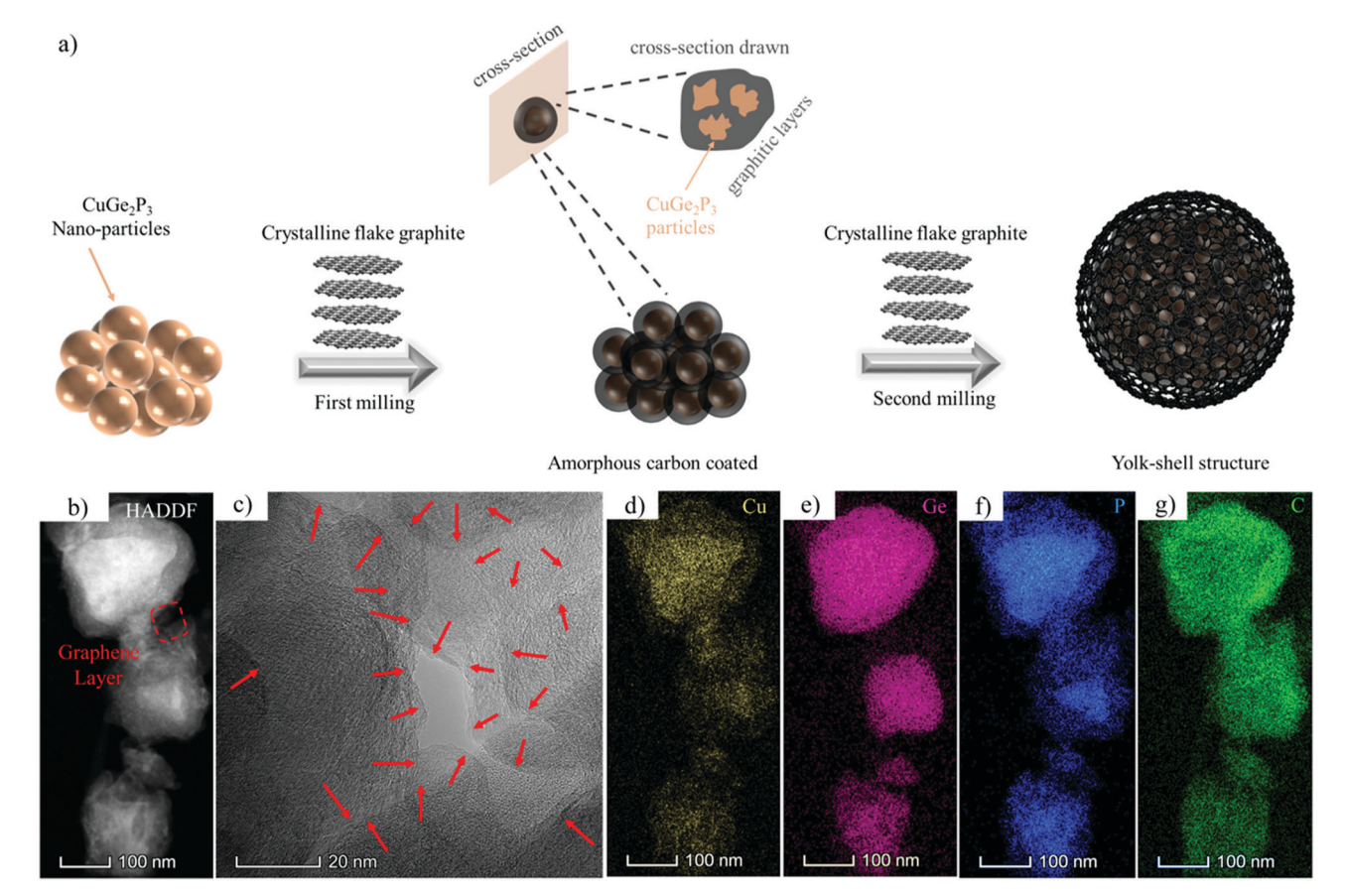
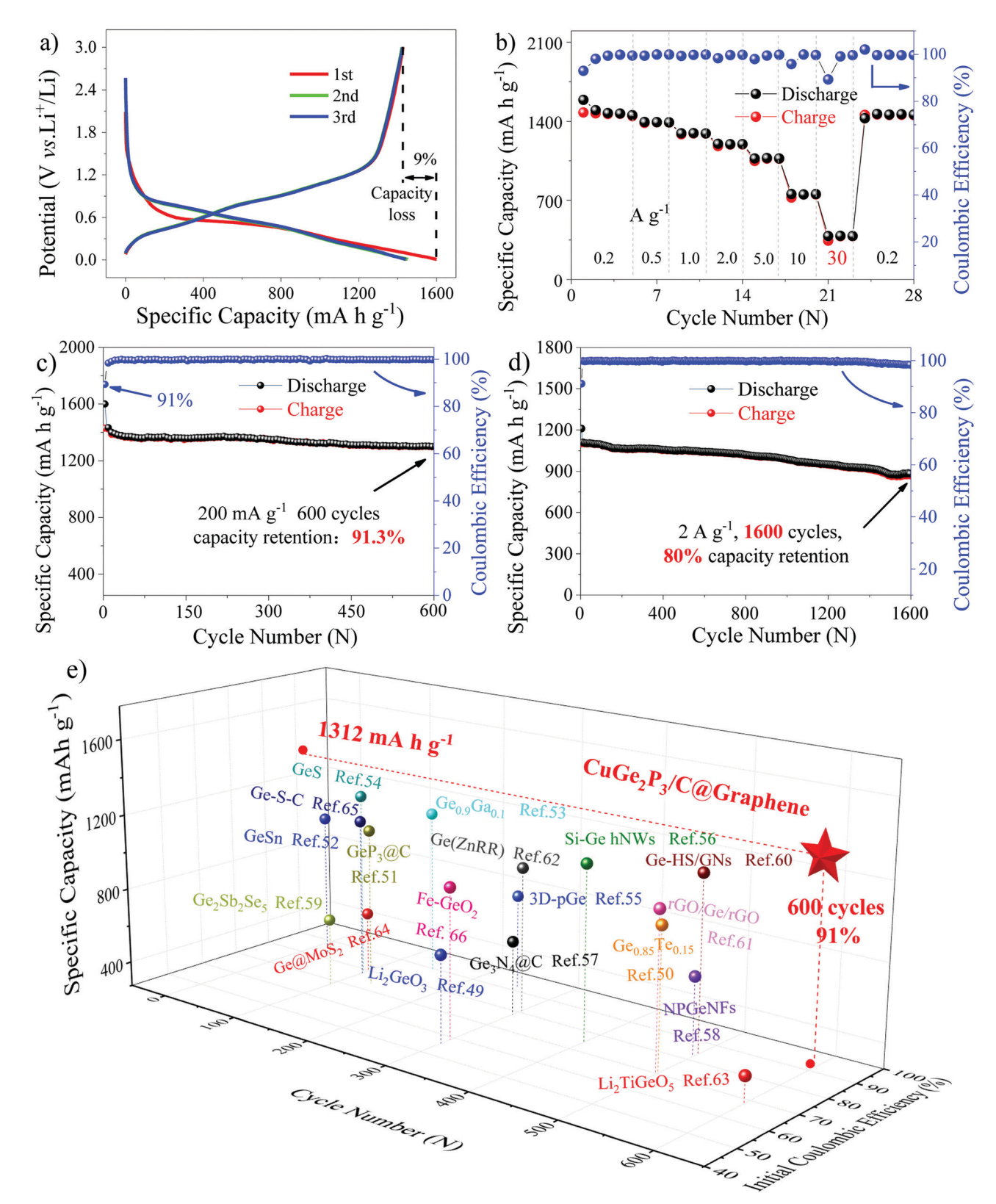


Fig. 5 The synthesis and characterization of the yolk-shell structured amorphous carbon coated CuGe<sub>2</sub>P<sub>3</sub> nanocomposite: (a) the scheme of the twostage ball milling process; (b) low-magnification TEM image; (c) HRTEM images of the marked red rectangle in (b); and (d-g) elemental mapping.

initial charge capacity, thus suggesting its excellent cycling stability. Compared with the fresh CuGe<sub>2</sub>P<sub>3</sub> electrode, the composite electrode (with carbon) showed slightly lower initial coulombic efficiency, which can be attributed to the slightly increased specific surface area (Fig. S24, ESI†) and solid electrolyte interface (SEI). At 2 A g<sup>-1</sup>, the CuGe<sub>2</sub>P<sub>3</sub>/C@Graphene delivers 876 mA h g<sup>-1</sup> capacity after 1600 cycles with the retaining capacity ratio up to 80%, suggesting its robust cycling stability, as presented in Fig. 6d. When evaluated for rate performance (Fig. 6b), the CuGe<sub>2</sub>P<sub>3</sub>/C@Graphene still shows 1464, 1392, 1287, 1167, 1068, 784 mA h g<sup>-1</sup> when the current density was increased from  $0.2~{\rm A~g}^{-1}$  to  $10~{\rm A~g}^{-1}$ . Surprisingly, at 30 A  ${\rm g}^{-1}$ , it still can offer 382 mA h g<sup>-1</sup> capacity, which is still larger than the theoretical capacity (372 mA h g<sup>-1</sup>) of the currently utilized graphite anodes. Once the current rate returned to 200 mA g<sup>-1</sup>, the initial reversible capacity of 1457 mA h g<sup>-1</sup> also bounced back. These performances shown by the CuGe<sub>2</sub>P<sub>3</sub>/C@Graphene anode surpassed the most recently reported Ge-based anode materials in terms of long cycling stability, high initial coulombic efficiency and large remained capacity, as shown in Fig. 6e (Table S5, ESI†). 49-66 The ultrahigh performance mainly profits from the following aspects: (1) inherently ultrafast Li-ionic and electronic conductivities of the cation-disordered CuGe<sub>2</sub>P<sub>3</sub> compound; (2) the reversible Li-storage mechanism along with superior electrochemical intermediates; and (3) the bi-carbon protection

strategy. To demonstrate the practical application potential of the CuGe<sub>2</sub>P<sub>3</sub>/C@Graphene anodes, we assembled a full cell using a LiFePO<sub>4</sub> cathode and our CuGe<sub>2</sub>P<sub>3</sub>/C@Graphene composite anode. Specifically, the anode loading was about 3 mg cm<sup>-2</sup> and the anode capacity was slightly (1.1 times) larger than the cathode capacity to avoid the lithium dendrite growth. As shown in Fig. S25 (ESI†), the full cell can be cycled over 20 cycles without capacity degradation, thus confirming its applicability to practical applications.

Taking the cation-disordered structural flexibility into account, we continue to expand the horizon to contain a new class of cation-disordered Cu(Zn)-Ge-P series compounds based on the CuGe<sub>2</sub>P<sub>3</sub> case and further evaluate them as anodes for LIBs. First of all, concerning the cation-disordered characteristic of the as-prepared CuGe<sub>2</sub>P<sub>3</sub>, series compounds with various cationic ratios (Cu/Ge ratios) were prepared using the similar ball milling method. As presented in Fig. 7a and Fig. S26a (ESI†), with an increase in the content of Ge locating at the cationic sites of the Cu-Ge-P series compounds, all these Ge-like diffraction peaks (CuGe<sub>2</sub>P<sub>3</sub> → CuGe<sub>3</sub>P<sub>4</sub> → CuGe<sub>4</sub>P<sub>5</sub>) only slightly shift to lower angles, suggesting these newly-formed compounds own a similar crystal structure, although with a little expansion because of the larger atomic size of Ge compared with that of Cu. Besides, as known, Zn locates at the right side of Cu in the Periodic Table of elements and, furthermore, as a noncompetitive metal with those



 $\textbf{Fig. 6} \quad \textbf{Electrochemical Li-storage performance of } \textbf{CuGe}_2P_3/\textbf{C@Graphene: (a) first three discharge-charge profiles; (b) rate performance; (c) cycling \\ \textbf{Current} \quad \textbf{Curre$ stability at 200 mA  $g^{-1}$ ; (d) cycling stability at 2 A  $g^{-1}$ ; and (e) performance comparison of the yolk–shell structured amorphous carbon coated CuGe<sub>2</sub>P<sub>3</sub> nanocomposite (CuGe<sub>2</sub>P<sub>3</sub>/C@Graphene) with the recently reported Ge-based anodes in the light of first coulombic efficiency and long cycling stability.

popular cathodes, it also contributes towards capacity when applied in LIBs. In the light of above merits and its comparable atomic size, bonding feature and electronegativity to Cu counterparts, we replace Cu with Zn to extend the family and simultaneouly alter the cationic ratios of Zn/Ge. Just like we planned, the Zn-Ge-P (ZnGe $_2$ P $_3$   $\rightarrow$  ZnGe $_3$ P $_4$   $\rightarrow$  ZnGe $_4$ P $_5$ ) present similar structural features (Fig. 7c, d and Fig. S26b, ESI $^{\dagger}$ ) to the above Cu-Ge-P compound counterparts. All results suggest that these cation-disordered arrangements at the atomic scale seem to involve with homologous atoms in a large range. As known, the micro-structures and components of materials determine their physicochemical properties including the electrochemical

performance and in the meanwhile elemental doping can also exert a significant influence on physicochemical properties. Therefore, we further evaluate the Li-storage behaviors of the above-prepared Cu(Zn)–Ge–P family compounds. As presented in Fig. 7e–g and Fig. S27 (ESI $^{\dagger}$ ), all the cation-disordered anode materials deliver large reversible capacities between 1400 mA h g $^{-1}$  and 1650 mA h g $^{-1}$  (Fig. 7f), which are close to their theoretical capacities on the basis of the terminal Li-alloy products of Li<sub>3.75</sub>Ge, Li<sub>3</sub>P and LiZn, with high first coulombic efficiency more than 90% (Fig. 7e). More interestingly, all these anodes present an appropriately low and safe working potentials ranging from 0.35 V to 0.55 V  $\nu$ s. Li $^{\dagger}$ /Li (Fig. 7g and Fig. S28, ESI $^{\dagger}$ ). All these

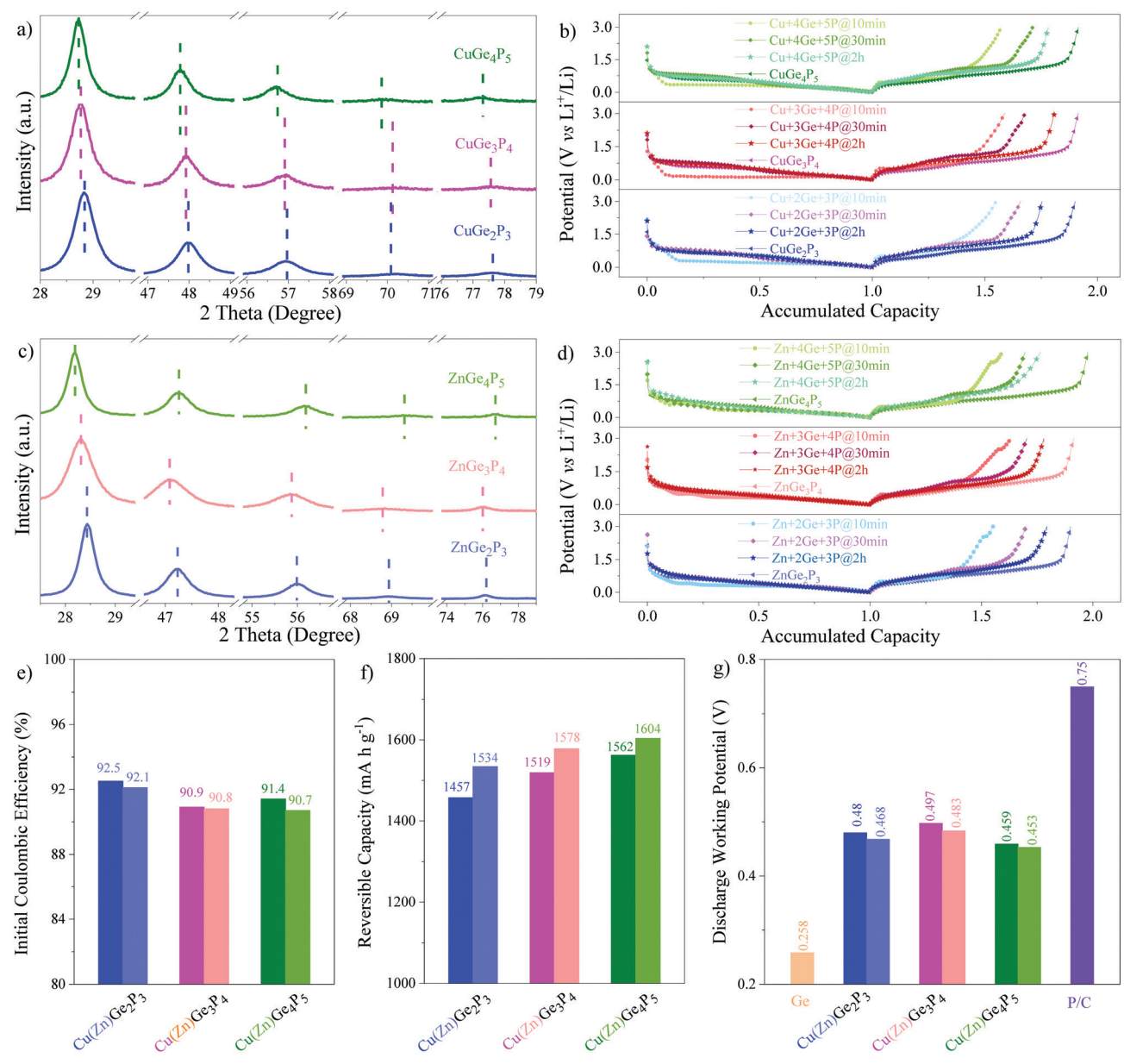


Fig. 7 (a) XRD patterns of cation-disordered Cu–Ge–P series compounds (CuGe<sub>2</sub>P<sub>3</sub>  $\rightarrow$  CuGe<sub>3</sub>P<sub>4</sub>  $\rightarrow$  CuGe<sub>4</sub>P<sub>5</sub>); (b) first-cycle galvanostatic discharge-charge profiles of the mechanically milled Cu–Ge–P series compounds at 0.2 A g<sup>-1</sup>; (c) XRD patterns of cation-disordered Zn–Ge–P series compounds (ZnGe<sub>2</sub>P<sub>3</sub>  $\rightarrow$  ZnGe<sub>3</sub>P<sub>4</sub>  $\rightarrow$  ZnGe<sub>4</sub>P<sub>5</sub>); (d) first-cycle galvanostatic discharge-charge profiles of the ball milled Zn–Ge–P samples at 0.2 A g<sup>-1</sup>; and (e–g) initial coulombic efficiency, reversible capacity and discharge working potential of the cation-disordered Cu(Zn)–Ge–P series compounds.

working potentials are above Li-plating potentials, thus avoiding the growth of Li-dendrites, which impale separators especially at large current rates. These working potentials of the newly formed family of anode materials are all appropriately lower than those of their phosphorus carbon composite counterpart, thus realizing higher energy density when served in a full battery. Consequently, we find a new class of cation-disordered Cu(Zn)-Ge-P electrode candidate materials with more practical potentials, which fill the gap between the Ge and P anodes, thus simultaneously meeting the standards of high safety as well as high-energy density when served in a full battery.

In conclusion, we have prepared a cation-disordered CuGe<sub>2</sub>P<sub>3</sub> compound using a simple and scalable mechanical ball milling process and demonstrated its ultrahigh performance as an advanced anode material for LIBs. The superior performance can be attributed to its Li-inert Cu constituent<sup>67</sup> and stronger resistance against volume variation during cycling, as validated by first-principles calculations and experimental measurements. The cation-disordered CuGe<sub>2</sub>P<sub>3</sub> experienced a reversible Li-storage mechanism of conversion reaction, as revealed by various characterization studies including ex situ high-resolution synchrotron X-ray diffraction, XRD, HRTEM along with SAED, XPS, and Raman spectroscopy. When hybridized with graphite, the constructed CuGe<sub>2</sub>P<sub>3</sub>/C@Graphene offers a reversible capacity of 1464 mA h g<sup>-1</sup> with an initial coulombic efficiency up to 91% and still retained 1312 mA h g<sup>-1</sup> capacity after 600 cycles at a current rate of 0.2 A g<sup>-1</sup>. When cycled at 2 A g<sup>-1</sup>, a reversible capacity of 876 mA h g<sup>-1</sup> was still retained after 1600 cycles. Furthermore, remarkable rate performance has also been demonstrated; the composite delivered up to 384 mA h g<sup>-1</sup> capacity at an ultrahigh current of 30 A g<sup>-1</sup>. The above Li-storage performance surpasses that of most Ge-based anodes ever reported. Moreover, it is found that a class of novel cationdisordered Cu(Zn)-Ge-P compounds with different cation ratios can be prepared using the same method, which have shown similar performance: large reversible capacity, high initial coulombic efficiency, suitable operating potential, and enhanced safety and energy density. These electrode materials are promising to be the next-generation anode materials with ultrahigh performance.

## **Experimental section**

#### Material preparation

As a typical synthesis procedure, red P, Cu and Ge powders in a molar ratio of 3:1:2 were thoroughly mixed using a planetary mechanical ball milling at 400 rpm for a certain number of hours in argon to obtain pure cation-disordered CuGe<sub>2</sub>P<sub>3</sub> powders. Stainless steel tank of 300 ml along with stainless steel hard alloy balls of  $\Phi$  5 mm was utilized for mechanical ball milling. The mass ratio of grinding balls to raw material was 20:1. For CuGe<sub>2</sub>P<sub>3</sub>/C@Graphene nanocomposite (weight ratio of C: CuGe<sub>2</sub>P<sub>3</sub> is 2:7), a two-stage ball milling process was carried out. Firstly, one half of the required graphite was poured and ground with the lab-prepared CuGe<sub>2</sub>P<sub>3</sub> for 10 h to achieve the well encapsulating of CuGe<sub>2</sub>P<sub>3</sub>. Then, the other half of the required graphite was poured and reground for another 1 h to enhance the electronic conductivity of the nanocomposite. Other cation-disordered Cu(Zn)-Ge-P compounds were prepared under similar mechanical ball milling experimental conditions.

#### Material characterization

We characterized the as-synthesized samples using an X-ray diffractometer (XRD, Bruker D8 ADVANCE) and a Raman spectrometer (HORIBA Jobin Yvon\*/LabRAM HR Evolution) with a 532 nm excitation laser. We investigated the crystalline structure of the as-prepared samples further utilizing synchrotron radiation source ( $\lambda = 0.2362 \text{ Å}$ ) at Beamline 28-ID-2 at National Synchrotron Light Source II (NSLS-II) at Brookhaven National Laboratory, Upton, NY. We observed the morphologies and microstructures of the as-prepared samples using a field-emission scanning electron microscope (FESEM, Hitach SU8220) and a high-resolution field-emission transmission electron microscope (HRTEM, FEI, Thermo Talos F200S) as well as an ASAP 2460 Surface Area Analyzer, respectively. We obtained the X-ray photoelectron spectroscopy (XPS) data using a Thermo Fisher Escalab 250Xi electron spectrometer. We collected the data on the thermal stability using a high temperature synchronous analyzer (TGA/ DSC3+, Switzerland).

#### **Electrochemical characterization**

We fabricated pure phase Cu(Zn)-Ge-P electrode films by coating the slurry of 70 wt% active materials, 10 wt% Li-PAA binder and 20 wt% carbon black as the electronic conductivity agent on a current collector of Cu foil and then drying at 70 °C overnight under vacuum. For CuGe2P3/C@Graphene and cation-disordered CuGe<sub>2</sub>P<sub>3</sub> samples, we prepared electrode films by only coating the slurry containing 90 wt% active materials, and 10 wt% Li-PAA binder on current collector of Cu foil without using any conductive agents. We assembled the CR2032 coin-type cells in a glove box filled with Ar ( $H_2O < 0.03$  ppm,  $O_2 < 0.05$  ppm, Mbraun, Labmaster 130) using Li metal as both the counter and reference electrodes, 1 M LiPF<sub>6</sub> in EC/DEC/EMC (1:1:1 by volume) as electrolytes, and Celgard 2325 as separators. The areal mass loading was about 1-1.5 mg cm<sup>-2</sup>. We conducted electrochemical tests using a LAND battery tester (Wuhan Kingnuo Electronic Co., China), a battery testing system (Hokuto Denko, HJ1001SD8) and electrochemical workstation (Autolab, Pgstat 302N). In addition, electrochemical impedance spectroscopy (EIS) tests were carried out in a frequency range from 100 kHz to 0.01 Hz. All tests were performed at a constant temperature of 25 °C. The gravimetric specific capacity was evaluated based on the mass of active materials.

#### Calculations detail

We performed theoretical calculations using the Vienna Ab-initio Simulation Package (VASP).<sup>68</sup> We applied the exchange correlation functional with generalized gradient approximation proposed by Perdew, Burke and Ernzerhof. The inner core-electrons were frozen by virtue of projector augmented wavefunction, with outer valence electron configuration of P 3s<sup>2</sup>3p<sup>3</sup>, Ge 3d<sup>10</sup>4s<sup>2</sup>4p<sup>2</sup>, and Cu 3d<sup>10</sup>4s<sup>1</sup>.

Paper

We utilized the  $4 \times 4 \times 4$  Monkhorst–Pack reciprocal grid, together with a 400 eV energy cutoff, was used for sufficient energy calculations. We also applied Gaussian smearing with smearing width (0.05 eV) to speed up the computation of electronic energy close to Fermi level.

## Conflicts of interest

There are no conflicts to declare.

## Acknowledgements

This work was supported by the National Natural Science Foundation of China (No. 21701030), and US National Science Foundation (DMR-1742828). All authors acknowledge the facilities applications of Georgia Institute of Technology, Guangdong University of Technology as well as National Taiwan Normal University. We also acknowledged the useful simulations discussions from Dr. Le Huang at Guangdong University of Technology.

### References

- 1 K. H. Seng, M. H. Park, Z. P. Guo, H. K. Liu and J. Cho, Angew. Chem., 2012, 51, 5657–5661.
- 2 X. Wang, L. Fan, D. Gong, J. Zhu, Q. Zhang and B. Lu, Adv. Funct. Mater., 2016, 26, 1104–1111.
- 3 H. Kim, Y. Son, J. Lee, M. Lee, S. Park, J. Cho and H. C. Choi, *Chem. Mater.*, 2016, 28, 6146–6151.
- 4 M. H. Seo, M. Park, K. T. Lee, K. Kim, J. Kim and J. Cho, *Energy Environ. Sci.*, 2011, **4**, 425–428.
- 5 Q. Ai, Q. Fang, J. Liang, X. Xu, T. Zhai, G. Gao, H. Guo, G. Han, L. Ci and J. Lou, *Nano Energy*, 2020, 72, 104657.
- 6 Y. Sun, S. Jin, G. Yang, J. Wang and C. Wang, ACS Nano, 2015, 9, 3479–3490.
- 7 C. Yan, W. Xi, W. Si, J. Deng and O. G. Schmidt, *Adv. Mater.*, 2013, 25, 539–544.
- 8 S. Liu, J. Feng, X. Bian, Y. Qian, J. Liu and H. Xu, Nano Energy, 2015, 13, 651–657.
- 9 H. Kim, Y. Son, C. Park, J. Cho and H. C. Choi, *Angew. Chem.*, 2013, 52, 5997–6001.
- 10 D. Li, H. Wang, H. K. Liu and Z. Guo, *Adv. Energy Mater.*, 2016, **6**, 1501666.
- 11 Y. Chen, C. Yan and O. G. Schmidt, *Adv. Energy Mater.*, 2013, 3, 1269–1274.
- 12 C. Kim, G. Song, L. Luo, J. Y. Cheong, S. H. Cho, D. Kwon, S. Choi, J. W. Jung, C. M. Wang, I. D. Kim and S. Park, *ACS Nano*, 2018, **12**, 8169–8176.
- 13 A. C. Serino, J. S. Ko, M. T. Yeung, J. J. Schwartz, C. B. Kang, S. H. Tolbert, R. B. Kaner, B. S. Dunn and P. S. Weiss, *ACS Nano*, 2017, 11, 7995–8001.
- 14 X. Li, Z. Yang, Y. Fu, L. Qiao, D. Li, H. Yue and D. He, *ACS Nano*, 2015, **9**, 1858–1867.
- 15 J. Ryu, J. H. Seo, G. Song, K. Choi, D. Hong, C. Wang, H. Lee, J. H. Lee and S. Park, *Nat. Commun.*, 2019, **10**, 2351.

- 16 K. C. Klavetter, J. P. d. Souza, A. Hellera and C. B. Mullins, J. Mater. Chem. A, 2015, 3, 5829–5834.
- 17 P. R. Abel, K. C. Klavetter, K. Jarvis, A. Heller and C. B. Mullins, J. Mater. Chem. A, 2014, 2, 19011–19018.
- 18 T. Li, C. Lim, Y. Cui, X. Zhou, H. Kang, B. Yan, M. L. Meyerson, J. A. Weeks, Q. Liu, F. Guo, R. Kou, Y. Liu, V. D. Andrade, F. D. Carlo, Y. Ren, C. J. Sun, C. B. Mullins, L. Chen, Y. Fu and L. Zhu, J. Mater. Chem. A, 2020, 8, 750–759.
- 19 P. R. Abel, K. C. Klavetter, A. Heller and C. B. Mullins, *J. Phys. Chem. C*, 2014, **118**, 17407–17412.
- 20 P. R. Abel, A. M. Chockla, Y. M. Lin, V. C. Holmberg, J. T. Harris, B. A. Korgel, A. Heller and C. B. Mullins, *ACS Nano*, 2013, 7, 2249–2257.
- 21 W. Xiao, J. Zhou, L. Yu, D. Wang and X. W. Lou, *Angew. Chem.*, 2016, **55**, 7427–7431.
- 22 C. C. Li, B. Wang, D. Chen, L. Y. Gan, Y. Zhang, Y. Yang, H. Geng, X. Rui and Y. Yu, ACS Nano, 2020, 14, 531–540.
- 23 D. Duveau, B. Fraisse, F. Cunin and L. Monconduit, *Chem. Mater.*, 2015, 27, 3226–3233.
- 24 N. Bensalah, M. Matalkeh, N. K. Mustafa and H. Merabet, *Phys. Status Solidi A*, 2020, **217**, 1900414.
- 25 W. Li, H. Li, Z. Lu, L. Ke, L. Gan, T. Zhai and H. Zhou, *Energy Environ. Sci.*, 2015, **8**, 3629–3636.
- 26 W. Li, X. Li, J. Yu, J. Liao, B. Zhao, L. Huang, A. Abdelhafiz, H. Zhang, J. H. Wang, Z. Guo and M. Liu, *Nano Energy*, 2019, 61, 594–603.
- 27 D. Kim, K. Zhang, M. Cho and Y. M. Kang, *Energy Environ. Sci.*, 2019, **12**, 1326–1333.
- 28 J. H. Kim, J. H. Yun and D. K. Kim, *Adv. Energy Mater.*, 2018, **8**, 1703499.
- 29 Y. Wei, L. Huang, J. He, Y. Guo, R. Qin, H. Li and T. Zhai, *Adv. Energy Mater.*, 2018, **8**, 1703635.
- 30 J. R. Rodriguez, Z. Qi, H. Wang, M. Y. Shalaginov, C. Goncalves, M. Kang, K. A. Richardson, J. G. Sanchez, M. G. M. Armenta and V. G. Pol, *Nano Energy*, 2020, 68, 104326.
- 31 Y. Wei, L. Huang, J. Chen, Y. Guo, S. Wang, H. Li and T. Zhai, *ACS Appl. Mater. Interfaces*, 2019, **11**, 41374–41382.
- 32 M. Li, Z. Zhang, X. Ge, Z. Wei, Y. Yao, H. Chen, C. Wang, F. Du and G. Chen, *Chem. Eng. J.*, 2018, **331**, 203–210.
- 33 S. Yuvaraj, K. Karthikeyan and R. K. Selvan, *J. Colloid Interface Sci.*, 2017, **498**, 76–84.
- 34 G. H. Lee, M. C. Sung, J. C. Kim, H. J. Song and D. W. Kim, *Adv. Energy Mater.*, 2018, **8**, 1801930.
- 35 L. Fu, X. Zheng, L. Huang, C. Shang, K. Lu, X. Zhang, B. Wei and X. Wang, *Nanoscale Res. Lett.*, 2018, **13**, 193.
- 36 J. Zhou, W. Zhang, H. Zhao, J. Tian, Z. Zhu, N. Lin and Y. Qian, *ACS Appl. Mater. Interfaces*, 2019, **11**, 22371–22379.
- 37 T. He, J. Feng, Y. Zhang, L. Zu, G. Wang, Y. Yu and J. Yang, *Adv. Energy Mater.*, 2018, **8**, 1702805.
- 38 L. Fu, C. Shang, J. Ma, C. Zhang, X. Zang, J. Chai, J. Li and G. Cui, *Sci. China-Mater.*, 2018, **61**, 1177–1184.
- 39 Y. Fu, Q. Wei, G. Zhang and S. Sun, Adv. Energy Mater., 2018, 8, 1702849.
- 40 W. Liu, H. Zhi and X. Yu, Energy Storage Mater., 2019, 16, 290-322.
- 41 W. Li, X. Li, J. Liao, B. Zhao, L. Zhang, L. Huang, G. Liu, Z. Guo and M. Liu, *Energy Environ. Sci.*, 2019, 12, 2286–2297.

**Paper** 

- 42 O. Crosnier, C. Mounsey, P. S. Herle, N. Taylor and L. F. Nazar, Chem. Mater., 2003, 15, 4890-4892.
- 43 S. Wenzel, S. Randau, T. Leichtweiß, D. A. Weber, J. Sann, W. G. Zeier and J. Janek, Chem. Mater., 2016, 28, 2400-2407.
- 44 N. Wu, Y. Li, A. Dolocan, W. Li, H. Xu, B. Xu, N. S. Grundish, Z. Cui, H. Jin and J. B. Goodenough, Adv. Funct. Mater., 2020, 30, 2000831.
- 45 G. K. Dey, R. T. Savalia, S. K. Sharma and S. K. Kulkarni, Corrosion Sci., 1989, 29, 823-831.
- 46 W. Li, J. Yu, J. Wen, J. Liao, Z. Ye, B. Zhao, X. Li, H. Zhang, M. Liu and Z. Guo, J. Mater. Chem. A, 2019, 7, 16785–16792.
- 47 S. Lebègue and O. Eriksson, Phys. Rev. B: Condens. Matter Mater. Phys., 2009, 79, 115409.
- 48 T. Wang, K. Zhang, M. Park, V. W. H. Lau, H. Wang, J. Zhang, J. Zhang, R. Zhao, Y. Yamauchi and Y. M. Kang, ACS Nano, 2020, 14, 4352-4365.
- 49 M. M. Rahman, I. Sultana, T. Yang, Z. Chen, N. Sharma, A. M. Glushenkov and Y. Chen, Angew. Chem., 2016, 55, 16059-16063.
- 50 Z. Yu, L. Yuan, Y. Wei, H. Li, X. Meng, Y. Li and F. Endres, Chem. Commun., 2019, 55, 10412-10415.
- 51 W. Qi, H. Zhao, Y. Wu, H. Zeng, T. Tao, C. Chen, C. Kuang, S. Zhou and Y. Huang, Sci. Rep., 2017, 7, 43582.
- 52 J. Doherty, S. Biswas, D. McNulty, C. Downing, S. Raha, C. O'Regan, A. Singha, C. O'Dwyer and J. D. Holmes, Chem. Mater., 2019, 31, 4016-4024.
- 53 E. J. Powell, S. M. Wood, H. Celio, A. Heller and C. B. Mullins, J. Mater. Chem. A, 2015, 3, 23442-23447.
- 54 Y. J. Cho, H. S. Im, H. S. Kim, Y. Myung, S. H. Back, Y. R. Lim, C. S. Jung, D. M. Jang, J. Park, E. H. Cha, W. I. Cho, F. Shojaei and H. S. Kang, ACS Nano, 2013, 7, 9075-9084.

- 55 T. Yoon, G. Song, A. M. Harzandi, M. Ha, S. Choi, S. Shadman, J. Ryu, T. Bok, S. Park and K. S. Kim, J. Mater. Chem. A, 2018, 6, 15961-15967.
- 56 K. Stokes, G. Flynn, H. Geaney, G. Bree and K. M. Ryan, Nano Lett., 2018, 18, 5569-5575.
- 57 C. Kim, G. Hwang, J. W. Jung, S. H. Cho, J. Y. Cheong, S. Shin, S. Park and I. D. Kim, Adv. Funct. Mater., 2017, 27, 1605975.
- 58 C. Kim, G. Song, L. Luo, J. Y. Cheong, S. H. Cho, D. Kwon, S. Choi, J. W. Jung, C. M. Wang, I. D. Kim and S. Park, ACS Nano, 2018, 12, 8169-8176.
- 59 J. R. Rodriguez, Z. Qi, H. Wang, M. Y. Shalaginov, C. Goncalves, M. Kang, K. A. Richardson, J. G. Sanchez, M. G. M. Armenta and V. G. Pol, Nano Energy, 2020, 68, 104326.
- 60 R. Mo, D. Rooney and K. Sun, Energy Storage Mater., 2020, 26, 414-422.
- 61 B. Wang, J. Jin, X. Hong, S. Gu, J. Guo and Z. Wen, J. Mater. Chem. A, 2017, 5, 13430-13438.
- 62 S. Choi, Y. G. Cho, J. Kim, N. S. Choi, H. K. Song, G. Wang and S. Park, Small, 2017, 13, 1603045.
- 63 Y. Liu, Q. Bai, A. M. Nolan, Y. Zhou, Y. Wang, Y. Mo and Y. Xia, Nano Energy, 2019, 66, 104094.
- 64 M. H. Hsieh, G. A. Li, W. C. Chang and H. Y. Tuan, J. Mater. Chem. A, 2017, 5, 4114-4121.
- 65 G. K. Sung and C. M. Park, J. Mater. Chem. A, 2017, 5, 5685-5689.
- 66 J. Wu, N. Luo, S. Huang, W. Yang and M. Wei, J. Mater. Chem. A, 2019, 7, 4574-4580.
- 67 M. N. Obrovac, L. Christensen, D. B. Le and J. R. Dahn, J. Electrochem. Soc., 2007, 154, A849-A855.
- 68 J. D. Pack and H. J. Monkhorst, Phys. Rev. B: Condens. Matter Mater. Phys., 1977, 16, 1748-1749.